

EARTHQUAKE-INDUCED FAILURE OF VOLCANIC EMBANKMENTS SUBJECTED TO PREVIOUS RAINFALL

Trong Nam Nguyen¹ and *Shima Kawamura²

^{1,2}Graduate School of Engineering, Muroran Institute of Technology, Japan

*Corresponding Author, Received: 13 Jan. 2022, Revised: 01 July 2022, Accepted: 02 Aug. 2022

ABSTRACT: Every year, slope failures such as landslides and debris flow on natural and artificial slopes cause great loss of life and property. The purpose of this study is to investigate the stability of the embankments constructed by coarse-grained volcanic soils under post-rainfall earthquakes like dual hazards in history (e.g., Typhoon Jebi and the 2018 Hokkaido Eastern Iwate earthquake). To accomplish the purpose, a series of 1g experiments on model slopes with Komaoka volcanic soils as material were performed using a spray nozzle and a shaking table. The experimental results showed that preceded rainfall greatly influences the stability of the embankment under subsequent earthquakes. Moreover, by comparing the result of this study with those of experiments on model embankments subjected to post-earthquake rainfall, it showed that the stability of the slope would change due to the different order of external force even if the previous shear strain induced is similar.

Keywords: Slope stability, Volcanic soil, Model test, Rainfall, Earthquake

1. INTRODUCTION

Distributed in many land areas of many countries, including Japan, volcanic soil (pyroclastic fall deposits or pyroclastic flow deposits) not only exist as natural slopes or grounds but also is widely utilized as road embankments or backfill. However, when subjected to disasters, volcanic slopes are very likely to cause failures because of their inherent properties. Owing to this, several researchers have investigated the mechanical and physical parameters of volcanic soils by element tests such as triaxial tests. For instance, Ng & Chiu [1] performed a series of triaxial tests and found out that saturated loose volcanic soils behave like clay or sand under different conditions of stress path. Nguyen et al. [2] conducted column tests and numerical analyses to investigate differences in the amount of infiltration and runoff water between bare and grassed volcanic soil. Miura et al. [3] clarified the mechanical behavior of coarse-grained volcanic soils in Hokkaido, Japan, and evaluated the effect of particle breakage on its mechanical behavior. However, studies on volcanic soil by modeling experiments are still very limited.

In recent years, global warming due to climate change has led to the frequent occurrence of far-than-expected heavy rainfall. In particular, rainfall, when combined with other effects such as cyclic loadings or freeze-thaw actions, will cause more unpredictable consequences, which attracts the attention of previous studies using various methods (e.g., the field monitoring results in [4], the model experiments in [5], the proposed early warning

criteria in [6], or overview of hazard events and research in [7]).

Post-rainfall earthquakes are not uncommon among those dual hazards in the past and have always caused large landslides, such as the 1968 Tokachi-oki earthquake and the 2004 Niigata Chuetsu earthquake. In particular, the 2018 Hokkaido Eastern Iwate earthquake that occurred after Typhoon Jebi has caused catastrophic ground disasters, as reported in the following literature. Kawamura et al. [8] analyzed the large-scale slope failure/landslide in the towns of Atsuma and Abira; including slope failure for a gentle slope, surface slope failure, river blockage, and rock slide. Besides, the mechanical and physical characteristics of the collapsed pyroclastic fall deposits spread over this area were also presented. Ishikawa et al. [9] reported road cracks and subsidence in Sapporo city, which was not observed in the 2003 Tokachi-oki earthquake of greater magnitude. One of the reasons for the difference in the damage situation between these two severe earthquakes suggested by the authors was the rainfall from Typhoon Jebi, which raised groundwater levels. Similarly, the effect of previous rainfall was also considered a potential factor in the scenario of the liquefaction phenomenon that occurred in the Satozuka district, Sapporo [10]. These disaster reports posed the need to experimentally verify the influence of antecedent rainfall on the earthquake resistance of embankments.

In this study, the mechanical behavior and failure phenomenon of the embankments constructed by Komaoka volcanic coarse-grained soil in Hokkaido, Japan, under previous rainfall and

subsequent seismic loadings were investigated based on the results of a series of 1g model experiments. In particular, the slope behavior under rainfall before the earthquake in this study will be compared with those in the case of the earthquake before rainfall in [5,11]. Thereby, the role of the order of external forces on the failure mechanism of the embankment is clarified.

2. TEST MATERIAL AND PROCEDURES

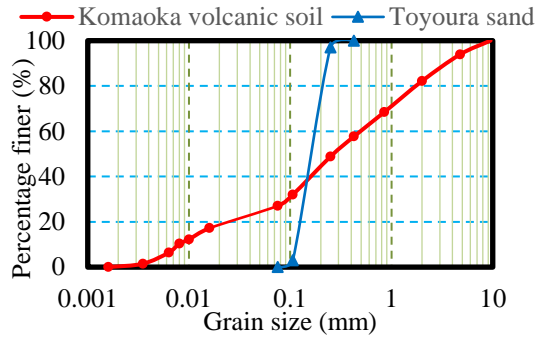


Fig.1 Grain size distribution of Spfl and Touyouura sand

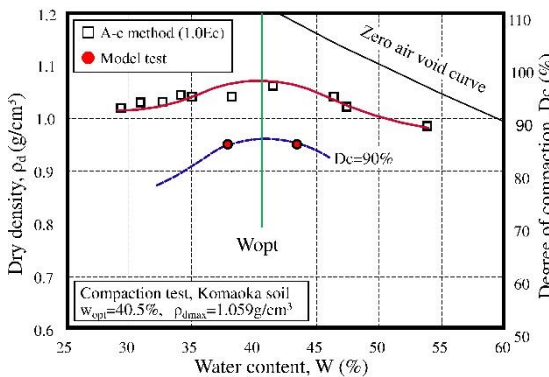


Fig.2 Compaction curve of Spfl for A-c method [12] and model test

The samples used in this study are Komaoka volcanic coarse-grained soils derived from Shikotsu caldera’s ejecta [3], hereafter referred to as Spfl. The physical properties and the grain size distribution of Spfl in comparison with those of Touyouura sand are shown in Table 1 and Fig.1, respectively. Fig.2 illustrates the compaction curve of Spfl obtained by the soil compaction A-c method of [12] (solid red line) and the compaction curve in model experiments (blue dotted lines). The curve showed that the optimum water content of Spfl is $w_{opt} = 40.5\%$. In Fig.2, symbols ● marked the test circumstances of the experiments in this study. A compaction degree of $D_c = 90\%$ ($\rho_d = 0.95 \text{ g/cm}^3$) was used to create the model slopes. In this study, the impact of rainfall and seismic loadings on the stability of slope was investigated in the case of

initial water content w_0 being equal to 37% and 43%, representing the dryer side and wetter side with the boundary being the optimum water content w_{opt} . Through comparison, the influence of the difference in initial water content during compaction in the same dry density condition on the slope failure phenomenon was investigated. The fluctuation in dry density during compaction was limited to 5% to reduce its effect on the slope behavior.

Table 1 Physical properties of Spfl and Touyouura sand

Physical properties	Spfl	Touyouura sand
ρ_s (g/cm ³)	2.47	2.68
e_{max}	2.25	0.96
e_{min}	1.21	0.64
D_{50} (mm)	0.27	0.16
U_c	46	1.5
F_c (%)	27	0

Note: D_{50} = mean grain size, U_c = coefficient of uniformity, and F_c = fines content.

The overall view of the test equipment used to investigate the slope behavior under rainfall and seismic loadings in this study is shown in Fig.3. The model soil tank’s inside dimensions are 2000mm in length, 700mm in height, and 600mm in width. The side of the tank was installed with 20mm thick tempered glass to allow monitoring of the deformation and phenomena occurring with the slope. This tank was attached with a one-dimensional vibration loading system. The hydraulic cylinder for this system was controlled by a computer to apply a regular wave (sinusoidal form) with a maximum load of 150 kg, an amplitude of $\pm 50 \text{ mm}$, and a frequency of 0.05Hz to 5.0Hz. The shaking table is 400mm long, 580mm wide, and 450mm high. The nozzle support system is adjustable in position and height to ensure that the entire slope can be exposed to rainfall. In addition, the valve system helps to regulate the rainfall intensity.

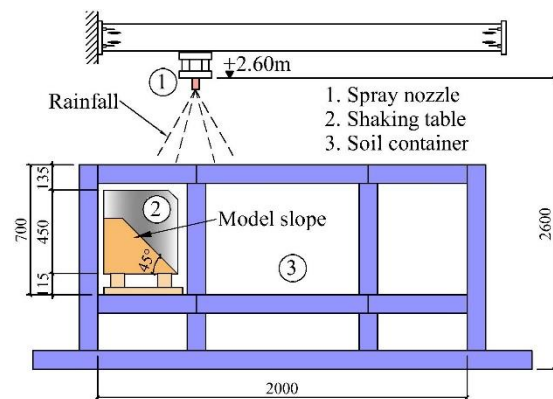


Fig.3 Overall view of apparatus

Fig.4 displays the shape of the model slopes and locations of measuring instruments. As shown in the figure, 3 acceleration meters (am1 to am3), 2 pore water pressure transducers (pw1, pw2), and 2 constant dielectric type soil-moisture meters (sm1, sm2) were placed inside model embankments. Phenomena on the front and side of the slope were recorded by 2 digital cameras. In this study, shear strain calculated from displacement of the kite strings, acceleration, pore water pressure, and saturation degree were measured as parameters for understanding the slope failure mechanism. Table 2 presents the conditions for experiments in this study.

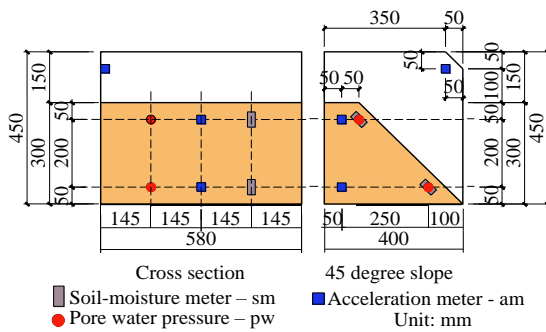


Fig.4 Slope dimensions and setting positions of measuring instruments

Kawamura and Miura [13] used the PIV method to monitor the failure phenomenon of model slopes and got the result that the saturation peaked when the shear strain was 4% to 6%, irrespective of the soil material, slope angle, difference in rainfall intensity, and the presence or absence of an impermeable layer; after that, the slope has collapsed. Therefore, the slope failure in this study is also defined as the moment when the shear strain γ reaches 6%. Kawamura et al. [14] used the results of consolidated undrained triaxial tests for Spfl to demonstrate the feasibility of using this soil in the prototype as the material of 1g model tests. In addition to the similarity laws presented in [14], the other scales necessary for this study were further calculated in Table 3.

Table 2 Test conditions in this study

Parameters	Value
Slope angle ($^{\circ}$)	45
Length of base (mm)	400
Initial water content (%)	37, 43
Dry density (g/cm^3)	0.95
Rainfall intensity (mm/h)	100
Acceleration (gal)	280, 320
Number of cycles	20
Pore water pressure condition before the earthquake	(i), (ii), (iii)

Note: (i) pw1 is higher than pw2; (ii) pw1 and pw2 reach the lowest value; (iii) pw2 is higher than pw1.

Table 3 Scaling of physical modeling for 1g model test used in this study

Parameters	Scale (m/p)
Length (L)	$1/\lambda$
Frequency (f)	$1/\lambda^{0.75}$
Acceleration (a)	1
Rainfall intensity (R)	$1/\lambda^{0.75}$
Pore water pressure (u)	$1/\lambda$
Effective overburden stress (σ_v')	$1/\lambda$
Saturation degree (Sr)	1

Note: m = model; and p = prototype.

3. TEST RESULTS AND DISCUSSIONS

In this study, the reduction in shear strength in the embankment was evaluated through the pore water pressure ratio $\Delta u/\sigma_{v0}'$, which is the change of pore water pressure Δu normalized by the initial effective overburden pressure σ_{v0}' . Along with it, the change of soil water content during the tests is illustrated by the saturation degree Sr normalized by the initial value Sr_0 .

3.1 Slope Collapse Mechanism Due to Rainfall

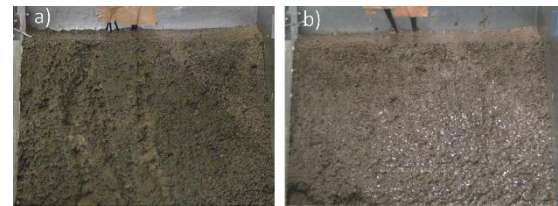


Fig.5 Front view of slope model during rainfall (a) $w_0=37\%$ (b) $w_0=43\%$

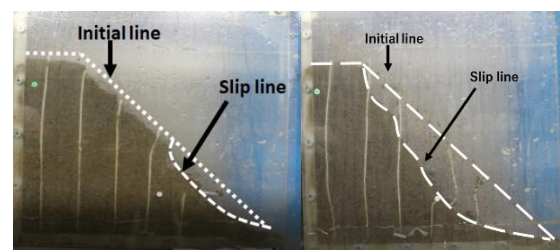


Fig.6 Failure shape of the model slope only by rainfall (a) $w_0=37\%$ (b) $w_0=43\%$

Kawamura and Miura [13] presented the influence of slope angle on the failure mechanism, while [11] clarified the effect of initial water content on the behavior of pore water pressure and saturation degree in volcanic slope during rainfall. In this study, the infiltration behavior of water inside the embankment was thoroughly investigated. Fig.5 shows the front view of the slope model during rainfall. Model slopes with initial water content $w_0=37\%$ were easily affected by surface

erosion, and gully erosion occurred. On the other hand, in the case of $w_0=43\%$, no gully erosion was observed, the surface flow was generated, and collapse happened from the base of the slope first and then gradually moved to the upper part, resulting in the whole collapse as shown in Fig.6.

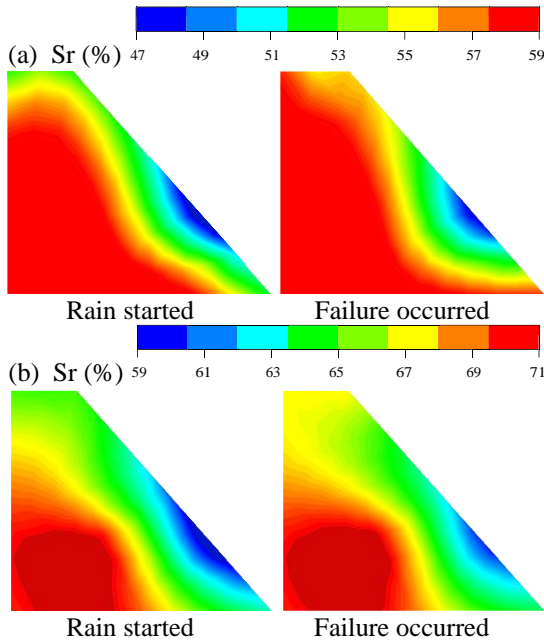


Fig.7 Distribution of Saturation degree inside the slope during rainfall (a) $w_0=37\%$ (b) $w_0=43\%$

To explain the above phenomenon, we measured and plotted the saturation degree distribution inside the model slope when the rain started and when the failure occurred (see Fig.7). For the case of $w_0=43\%$, there was only a slight increase in saturation degree in the surface, while inside the model slope, almost no change was observed, which proved that runoff was dominant over infiltration. In contrast, the case of $w_0=37\%$ showed a more significant increase in the saturation degree. This difficulty of rainwater in permeating the model slope with the water content of 43% compared to the case of 37% demonstrated that the permeability of compacted Komaoka volcanic soils reduces as the initial water content increases. This trend in the modeling experiment confirms the results of the hydraulic conductivity of Sp_{fl} in the permeability experiments in [15].

The process of saturation change during rainfall is shown in Fig.8. To provide enough information for the saturation degree distribution charts in Fig.7, in rainfall-only experiments in this study, six soil-moisture meters were used instead of two. The meter that reached the highest value was sm1 located near the crown (increase by 20%) in Fig.8(a), and sm5 installed near the basement of the model slope (increase by 2.5%) in Fig.8(b). In the

case of $w_0=37\%$, seepage easily occurred, as shown by the fact that the sm2 and sm4 values were approximately the same as sm3 and sm5, respectively. In contrast, in Fig.8(b), the sm6, sm4, and sm2 values were completely below sm5, sm3, and sm1.

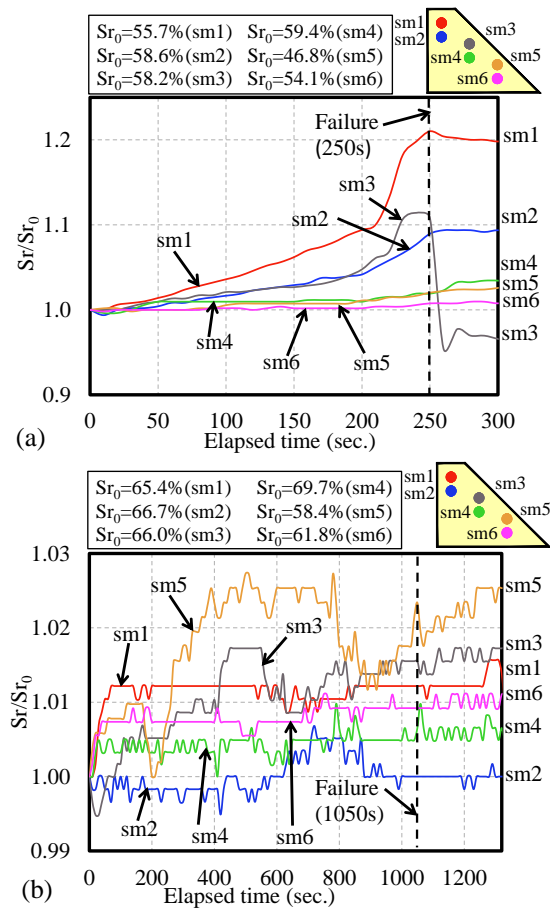


Fig.8 Changes in saturation degree during rainfall (a) $w_0=37\%$ (b) $w_0=43\%$

Regarding the change of pore water pressure shown in Fig.9, both cases of initial water content show a similar trend. When the rain started, the pore water pressure inside the embankment immediately increased due to seepage. In the case of $w_0=37\%$, transducer pw1 was placed in a similar position to sm1 and showed the same trend: sudden increase near failure time. This may be due to the increase in soil mass above the transducer and the decrease of suction with saturation. Kawamura et al. [14] indicated that Komaoka volcanic soil dissipates suction when the saturation degree is greater than around $Sr=60\%$ (under the wetting path). Pore water pressure ratio reached 1, and flowed deformation was also confirmed in the front camera. In contrast, in the case of $w_0=43\%$, at the time of failure, the pore water pressure ratio had not reached 1, and the front camera also recorded that the failure started due to erosion at the basement of

the slope.

Fig.10 shows the change of the rainfall-induced shear strain over time. In this figure, the shear strain generated in both cases increases non-linearly and the rate of this increase gets faster with time.

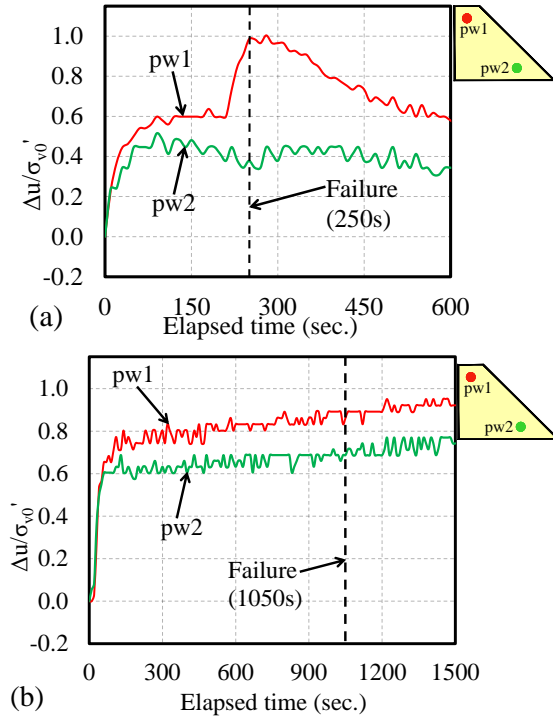


Fig.9 Changes in pore water pressure over time for the case of rainfall only (a) $w_0=37\%$ (b) $w_0=43\%$

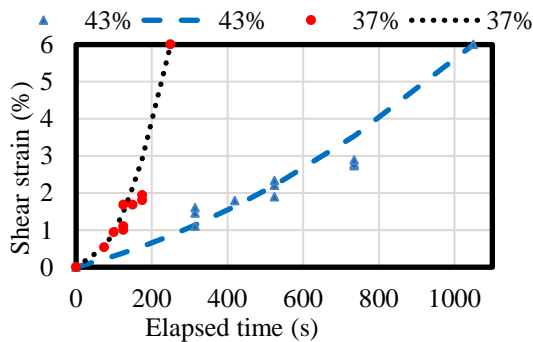


Fig.10 Changes in rainfall-induced shear strain over time

3.2 Behavior of Slope When Seismic Loading Applied After Rainfall

The cumulative rainfall up to the time of failure mentioned in section 3.1 is set as the total rainfall amount R_0 , which is equal to 7mm (100mm/h x 0.07h) for $w_0=37\%$ and 29mm (100mm/h x 0.29h) for $w_0=43\%$. In this section, the model slope was first subjected to the precipitation of $R=0.5R_0$. Since natural earthquakes can occur at any time after the

rainfall stops, we applied seismic loadings to the model slope according to 3 typical cases corresponding to 3 moments:

- Case (i): pw1 is higher than pw2;
- Case (ii): pw1 and pw2 reach the lowest value;
- Case (iii): pw2 is higher than pw1.

In which pw1 and pw2 are the pore water pressure at the crown and the basement of the embankment, respectively.

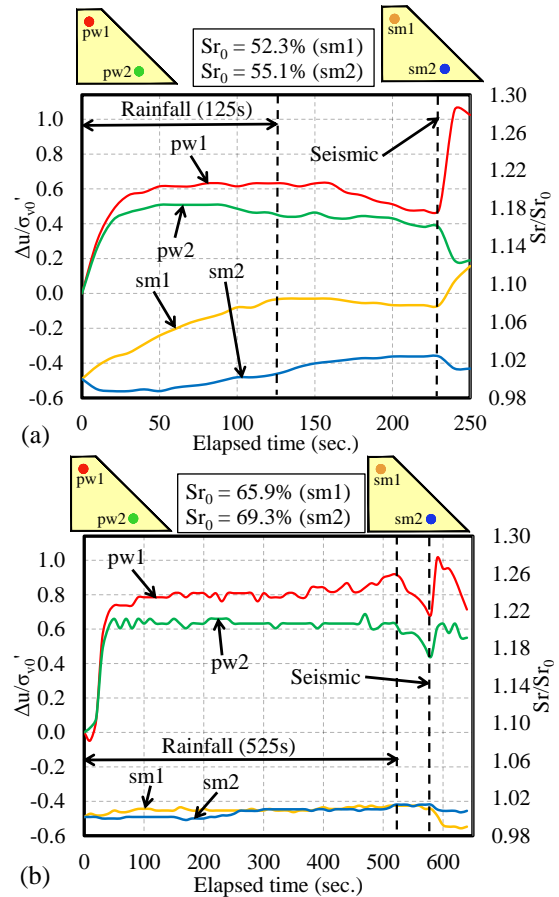


Fig.11 Changes in pore water pressure and saturation degree in the case of (i) (a) $w_0=37\%$ (b) $w_0=43\%$

Fig.11 shows the change of pore water pressure ratio and saturation degree ratio in the case of (i). During the rainfall, these behaviors remained similar to the rainfall-only tests. After the rainfall had stopped for about 60 to 100 seconds, seismic loadings were applied when the residual pore water pressure was still high. As can be seen in Fig.11, the pore water pressure of pw1 suddenly increased (compared to before the earthquake) and exceeded 1 in both cases due to the response characteristics and rapid seismic loadings. On the other hand, the pore water pressure of pw2 shows 2 different trends when subjected to 20 cycles: an increase in the case of $w_0=43\%$ and a decrease in the case of $w_0=37\%$. This is presumed to be due to the development of

negative excess pore water pressure under the effects of unsaturation and dilatancy. Similar to the pore water pressure, the saturation degree also showed a rapid change at the time of seismic loadings. The front view camera confirmed flow deformation at the crown of the slope in both initial water content and boiling sand in the case of $w_0=43\%$.

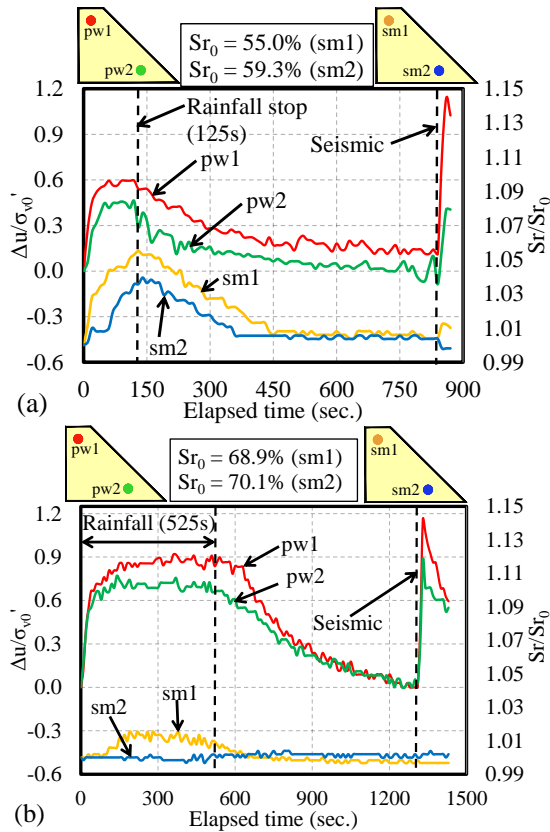


Fig.12 Changes in pore water pressure and saturation degree in the case of (ii) (a) $w_0=37\%$ (b) $w_0=43\%$

Next, in case (ii), the failure did not occur under an acceleration of 280 gals as in (i) and (iii) for both initial water contents. Therefore, the change in pore water pressure and saturation degree in the embankment upon failure under case (ii) was studied with an acceleration of 320 gals, as shown in Fig.12. Similar to case (i), the values of pw1 and pw2 decreased with the time from the end of rainfall. When the dissipation time was extended to about 10-15 min, the pore water pressure at both locations decreased to zero, and then the seismic loading test was carried out. Although both pw1 and pw2 in both initial water content cases had been at the lowest value before earthquakes, they changed immediately and showed an increasing trend after 20 cycles. The pw1 value exceeded 1, and flow deformation in the upper area was observed. A difference from case (i) is the appearance of

transverse cracks near the crown of the slope. Regarding the saturation degree when seismic loadings were applied, the case of $w_0=37\%$ showed a small change, while the case of $w_0=43\%$ showed almost no change.

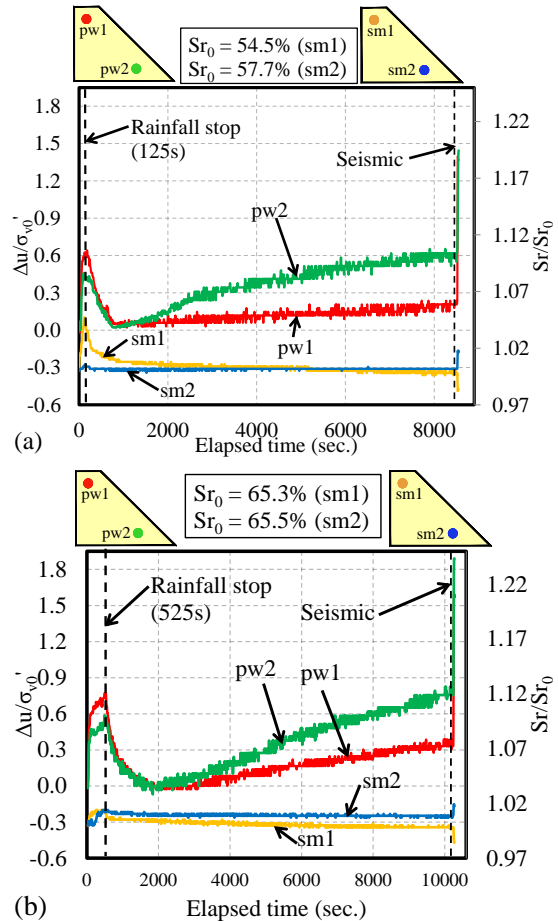


Fig.13 Changes in pore water pressure and saturation degree in the case of (iii) (a) $w_0=37\%$ (b) $w_0=43\%$

Finally, Fig.13 shows the change of pore water pressure and degree of saturation in case (iii). In more than 2 hours after the end of the rainfall, the pore water pressure decreased as in case (ii) and then increased again because the water penetrates the bottom of the embankment and the consolidation of the soil occurs over time. When seismic loadings were applied, both excess pore water pressure ratios of pw1 and pw2 exceeded 1 and showed greater values than cases (i) and (ii). Flow deformation was confirmed almost simultaneously in both the upper and lower parts of the slope. The cracks caused by seismic loading were longer than in case (ii) and appeared both at the crown and the upper part of the slope. Focusing on the degree of saturation, a trend is common for both initial water content: sm1 sharply increases and sm2 sharply decreases right after being

subjected to the seismic loadings.

3.3 Effect of Previous Rainfall on Earthquake-Induced Failure

Fig.14 shows the response acceleration at the crown area, basement area, and shaking table under 280 gals seismic loading in the earthquake-only experiments conducted in [11]. It can be seen that the value at the upper part of the slope is larger than that at other positions. This trend was also observed in all post-rainfall earthquake experiments performed in this study.

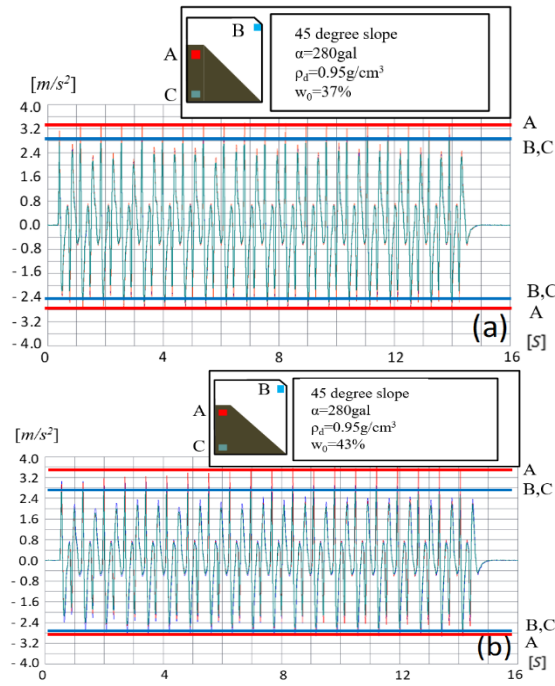


Fig.14 Variation of accelerations in the basement, the crown of the embankment, and shaking table (a) $w_0=37\%$ (b) $w_0=43\%$

Phenomenologically, when seismic loadings were applied to the soil that was still wet due to rainfall in case (i), failure occurred, but cracks did not appear. On the contrary, in cases (ii) and (iii), the soil has become drier, so the response of the embankment to seismic loadings is similar to that in the case without rainfall. Moreover, the length, width, and density of the cracks in cases (ii) and (iii) were larger than those in the case of earthquakes only. When the slope with the initial water content of 37% was subjected to the seismic without previous rainfall, the pore water pressure changed periodically. After the end of the loadings, it did not accumulate but returned to its original value. Thus, the slope still works within the elastic limit. In contrast, in the case of rainfall before the earthquake, accumulation in pore water pressure immediately occurred. It can be seen that the rainfall caused the

soil structure to separate and the soil to be plastically deformed. In the case of earthquake-only tests with $w_0=43\%$, the pore water pressure ratio exceeded 1, but the slope did not collapse after 20 cycles, which shows the cyclic mobility of the slope. Compared with the case of rainfall before seismic loadings, when the pore water pressure ratio exceeded 1, the slope collapsed

3.4 Effect of Pore Water Pressure Condition and Initial Water Content on Slope Failure

In this study, besides the rainfall amount of $R=0.5R_0$, we also performed other rainfall tests such as $0.3R_0$, $0.6R_0$, and $0.7R_0$ to get different shear strains with the model slope. After that, seismic loadings were applied and the different failure times were confirmed. Fig.15 shows the relationship between failure time caused by seismic loadings and the rainfall-induced shear strain under different conditions of pore water pressure. The seismic failure time in Fig.15 was normalized by Eq. (1).

$$R_{ft}^{r-s} = T_{fs} / T_{fs0} \quad (1)$$

where T_{fs} is the failure time due to seismic loadings of model slope that were subjected to previous rainfall, while T_{fs0} is the failure time due to seismic loadings only. From Fig.15, it can be seen that the seismic failure time decreases inversely proportional to the shear strain due to rainfall. When the initial water content is 37%, at the same shear strain, the failure time was the longest in case (ii), followed by that in case (iii), and the shortest failure time was in case (i). As mentioned above, the effect of dissipation or the residual pore water pressure existing in the slope cannot be ignored.

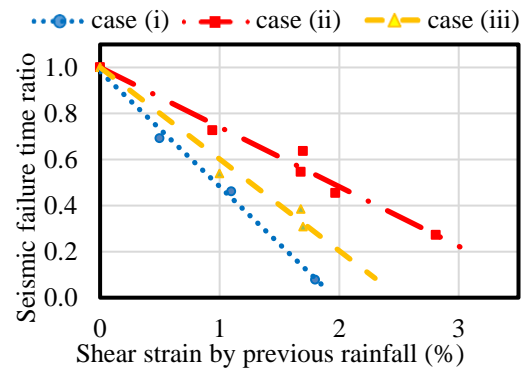


Fig.15 Relationship between seismic failure time ratio and rainfall-induced shear strain in different conditions of pore water pressure ($w_0=37\%$)

Similar to Fig.15, Fig.16 shows the change in collapse time due to seismic loading with the change in shear strain generated by previous rainfall

under different conditions of initial water contents. From the figure, it can be seen that for the same shear strain, $w_0=37\%$ had a shorter time until collapse than $w_0=43\%$, similar to the rainfall-only case. This is probably because the difference in infiltration and water retention behavior mentioned above affected the failure time.

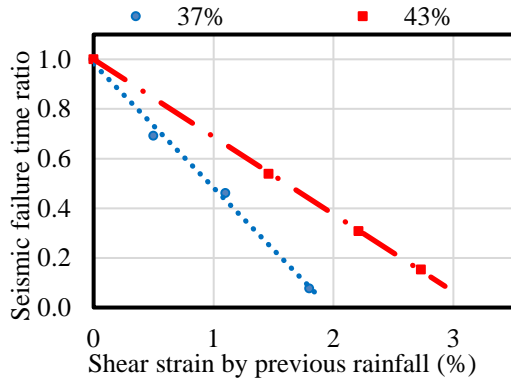


Fig.16 Relationship between the seismic failure time ratio and rainfall-induced shear strain in different initial water content in case (i)

3.5 Effects of Different Orders of Rainfall and Seismic Loadings on Slope Failures

In this section, the result of this study will be compared with the case where seismic loadings were applied before rainfall in [5,11]. Due to the difficulty in equally evaluating the effect of rainfall and seismic loadings, the failure time in the case of earthquake → rainfall will be normalized by Eq. (2) in the same way as the above section.

$$R_{fr}^{e-r} = T_{fr} / T_{fr0} \quad (2)$$

where T_{fr} is the failure time due to rainfall of model slope that was subjected to previous seismic loadings, while T_{fr0} is the failure time due to rainfall only. Fig.17 presents the relationship between failure time ratio and shear strain caused by previous external force in the 2 initial water content cases (data for rainfall → earthquake are taken according to case (i)).

When seismic loadings are applied first, the model slopes with the initial water content of 37% and 43% show 2 different trends. The failure time decreases as the shear strain generated by seismic loadings increases in the case of 37%. In the case of 43%, when the shear strain increases, the failure time still increases until γ reaches 4% and after that, it decreases. When rainfall is applied first, 2 initial water content model slopes show the same trend, and the failure time is shorter compared with the case of earthquake → rainfall for the same shear strain generated.

This difference can be explained as follows. In the case of a post-rainfall earthquake, the volumetric weight of the soil is increased by rainfall, which leads to the increase of the vertical driving forces in the slope. After that, seismic loadings will create horizontal driving force and further decrease the shear strength because the generated instantaneous pore water pressure superimposes the pore water pressure caused by the seepage flow. On the other hand, when seismic loadings are applied first, although they increase the pore water pressure, they also increase soil density due to the compaction effect. This will cause subsequent rainfall to take a longer time to loosen the soil structure to destabilize the slope. These results mentioned above lead to a need for appropriate evaluation of embankments under complex disasters taking into account the order of effects of external forces. However, the above results may change with variations in soil materials, test and measuring equipment, as well as inherent errors such as the scale effect. In any case, further discussions in this direction will be required.

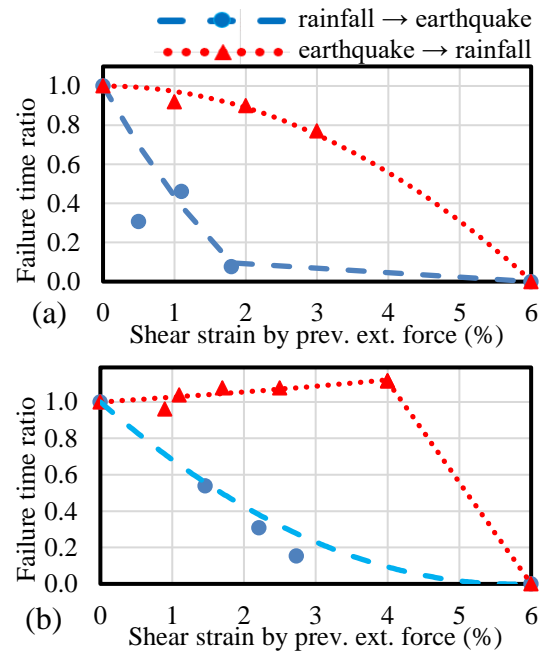


Fig.17 Relationship between failure time ratio and shear strain generated by previous external forces (a) $w_0=37\%$ (b) $w_0=43\%$

4. CONCLUSIONS

From a series of rainfall and earthquake experiments on model slopes using Komaoka volcanic coarse-grained soil, the following conclusions were obtained:

(1) The rainfall-induced residual pore water pressure and water retention condition inside the slope play an important role in evaluating the stability of embankments under subsequent

earthquakes.

(2) Initial water content has a great influence on the mechanical behavior, infiltration characteristics, and failure phenomenon of embankments due to rainfall and/or earthquakes.

(3) In studying the slope under complex hazards, even if the previous shear strain induced is similar, the stability of the slope may change due to the different order of rainfall and seismic loadings.

5. ACKNOWLEDGEMENTS

The authors wish to express their sincere gratitude to Mr. Y. Kusuda, Mr. R. Yamada, and Mr. K. Nakano (Muroran Institute of Technology, Japan), who conducted a major part of the experiments. This work was supported by JSPS KAKENHI (A) (Grant Number 20H00266) and JST SPRING (Grant Number JPMJSP2153) in Japan.

6. REFERENCES

- [1] Ng C.W.W. and Chiu A.C.F., Behavior of a Loosely Compacted Unsaturated Volcanic Soil, *Journal of Geotechnical and Geoenvironmental Engineering*, Vol. 127, Issue 12, 2001, pp. 1027–1036.
- [2] Nguyen T.B., Tatsuya I., and Srikrishnan S.S., Rainfall Infiltration and Runoff Characteristics of an Unsaturated Volcanic Soil under Grass Cover, in *PanAm Unsaturated Soils 2017, Second Pan-American Conference on Unsaturated Soils*, 2017.
- [3] Miura S., Yagi K., and Asonuma T., Deformation-Strength Evaluation of Crushable Volcanic Soils by Laboratory and In-Situ Testing, *Soils and Foundations*, Vol. 43, Issue 4, 2003, pp. 47–57.
- [4] Kawamura S., Miura S., Yokohama S., Kudo A., and Kaiya N., Field Monitoring of Embankment Constructed by Volcanic Soil and Its Evaluation, in *Geo-Congress 2013, American Society of Civil Engineers*, 2013.
- [5] Kawamura S., Miura S., Dao H.M., and Yamada R., Rainfall-Induced Failure of Volcanic Embankments Subjected to Cyclic Loadings in Cold Regions, in *Geo-China 2016, Geotechnical Special Publication, No.257, ASCE*, 2016, pp.116-123.
- [6] Zhu Y., Ishikawa T., Siva Subramanian S., and Luo B., Early warning system for rainfall- and snowmelt-induced slope failure in seasonally cold regions, *Soils and Foundations*, Vol. 61, Issue 1, 2021, pp. 198–217.
- [7] Baselt I. and Heinze T., Rain, Snow and Frozen Soil: Open Questions from a Pore-scale Perspective with Implications for Geohazards, *Geosciences*, Vol. 11, Issue 9, 2021, p. 375.
- [8] Kawamura S., Kawajiri S., Wataru H., and Watanabe T., Slope failures/landslides over a wide area in the 2018 Hokkaido Eastern Iburi earthquake, *Soils and Foundations*, Vol.59, 2019, pp.2376–2395.
- [9] Ishikawa T., Yoshimi M., Isobe K., and Yokohama S., Reconnaissance report on geotechnical damage caused by 2018 Hokkaido Eastern Iburi earthquake with JMA seismic intensity 7, *Soils and Foundations*, Vol. 61, Issue 4, 2021, pp. 1151–1171.
- [10] Watabe Y. and Nishimura S., Ground movements and damage in Satozuka district, Sapporo due to 2018 Hokkaido Eastern Iburi Earthquake, *Soils and Foundations*, Vol. 60, Issue 5, 2020, pp. 1331–1356.
- [11] Kawamura S. and Miura S., Stability of Volcanic Slopes in Cold Regions, *Journal of Geography and Geology*, Vol. 6, Issue 3, 2014, pp. 34-54.
- [12] Japanese Geotechnical Society (JGS), Test method for soil compaction using a rammer, JGS 0711-2009, Tokyo, JGS, 2009.
- [13] Kawamura S. and Miura S., Rainfall-induced failures of volcanic slopes subjected to freezing and thawing, *Soils and Foundations*, Vol. 53, Issue 3, 2013, pp. 443–461.
- [14] Kawamura S., Miura S., and Matsumura S., Stability Monitoring of Embankments Constructed by Volcanic Coarse-Grained Soil in Snowy-Cold Regions, *Journal of Cold Regions Engineering*, Vol. 35, Issue 1, 2021, p. 04020030.
- [15] Dao M.H., Stability evaluation on internal erosion of volcanic coarse-grained soil, Doctoral dissertation, Graduate School of Engineering, Muroran Institute of Technology, 2018.